J. Fluid Mech. (2023), *vol*. 975, A31, doi:10.1017/jfm.2023.887

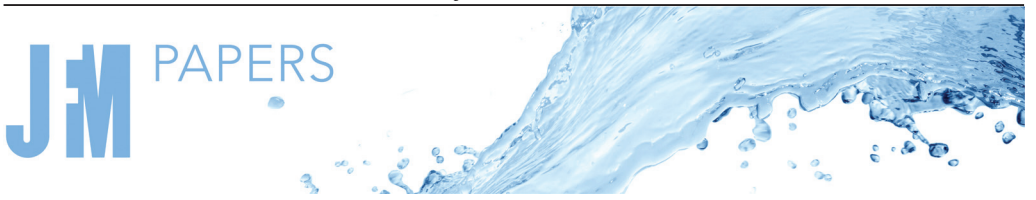

Slow motion of a sphere near a sinusoidal surface

Gaojin Li[1,2,†]

[1]State Key Laboratory of Ocean Engineering, Shanghai 200240, PR China

[2]School of Naval Architecture, Ocean and Civil Engineering, Shanghai Jiaotong University, Shanghai 200240, PR China

(Received 4 April 2023; revised 16 July 2023; accepted 17 October 2023)

Particle motion near non-plane surfaces can exhibit intricate hydrodynamics, making it an attractive tool for manipulating particles in microfluidic devices. To understand the underlying physics, this work investigates the Stokesian dynamics of a sphere near a sinusoidal surface, using a combination of perturbation analysis and boundary element simulation. The Lorentz reciprocal theorem is employed to solve the particle mobility near a small-amplitude surface. Compared with a plane wall, the curved topography induces additional translation and rotation velocity components, with the direction depending on the location of the sphere and the wavelength of the surface. At a fixed distance from the surface, the longitudinal and vertical mobilities of the sphere are strongly affected by the wavelength and amplitude of the surface, whereas its transverse mobility is only mildly influenced. When a sphere settles perpendicular to a sinusoidal surface, the far-field hydrodynamic effect drives the particle towards the local hill, while the near-field effect attracts the particle to the valley. These results provide valuable insights into the particle motion near surfaces with complex geometry.

Key words: stokesian dynamics

1. Introduction

Manipulation of particles and cells in microfluidic devices has long been of interest in chemical and biomedical applications, such as particle sorting (Sajeesh & Sen 2014), cell separation (Bhagat *et al.* 2010), chemical analysis (Jokerst, Emory & Henry 2012) and cell cultivation (Mehling & Tay 2014). Traditional approaches for particle manipulation often involve multiple physics (Cha *et al.* 2022), such as an inertial lift force (Zhang *et al.* 2016), electro-magnetic forces (Nam-Trung 2012; Zhang *et al.* 2014) and viscoelastic effects (Li, McKinley & Ardekani 2015; Yuan *et al.* 2017). Recent studies have demonstrated that the Stokesian hydrodynamics along in a confined flow also provides an effective way to passively separate and sort particles (Uspal, Eral & Doyle 2013; Georgiev *et al.* 2020).

† Email address for correspondence: gaojinli@sjtu.edu.cn

The trajectory of a particle in a viscous fluid is strongly influenced by its shape, position and orientation, as well as the geometry of container boundaries. To achieve more effective control over particles and cells, it is critical to develop a fundamental understanding of the hydrodynamics of particle motion near a surface.

The slow motion of particles in a viscous fluid, as commonly encountered in sedimentation and colloid suspensions, has long been studied as a fundamental problem in fluid dynamics. Since the pioneering work of Stokes (Stokes 1901), who analysed the flow past a sphere in an unbounded fluid, the hydrodynamics of particle movement under different flow conditions has been widely studied in the literature. For a sphere in an arbitrary background fluid flow, Faxén (1922) derived the general formulation for the hydrodynamic force and torque exerted on the sphere using Lamb's harmonic solution in a spherical coordinate system. Due to the linearity of the Stokes equation, the particle velocity and the applied force connected by linear relations $(\boldsymbol{U}, \boldsymbol{\Omega})^{\mathrm{T}} = \boldsymbol{M} \cdot (\boldsymbol{F}, \boldsymbol{T})^{\mathrm{T}}$ and $(\boldsymbol{F}, \boldsymbol{T})^{\mathrm{T}} = \boldsymbol{R} \cdot (\boldsymbol{U}, \boldsymbol{\Omega})^{\mathrm{T}}$, where $\boldsymbol{U}$ and $\boldsymbol{\Omega}$ are the particle's translational and rotational velocities, $\boldsymbol{F}$ and $\boldsymbol{T}$ are the external force and torque applied on the particle, and $\boldsymbol{M}$ and $\boldsymbol{R} = \boldsymbol{M}^{-1}$ are the mobility and resistance matrices. Determining the mobility and resistance matrices in various flow scenarios is the key task in the study of particle motion in the Stokes regime.

The Stokesian dynamics of a particle near a plane wall has been extensively studied for its close connection to industrial applications. Theoretical analyses often simplify the problem by focusing on either far-field or near-contact hydrodynamic interactions. When the particle is many times its radius from the wall, far-field analyses are commonly employed, using either singularity solutions (Blake & Chwang 1974; Chwang & Wu 1975) or the method of reflections (Smoluchowski 1911; Kynch 1959) to capture the far-field hydrodynamic interaction between the particle and the wall. In this regime, the particle translation can be approximated as a Stokeslet and is influenced by the induced image singularities due to the presence of the wall, while the higher-order singularities are less important. For a spherical particle, the drag force is $F = 6\pi\mu Ua(1 + 9a/8h)$ when its motion is perpendicular to the wall, and $F = 6\pi\mu Ua(1 + 9a/16h)$ for a parallel motion, where a is the sphere radius, h is the distance between the sphere centre and the wall, U is sphere velocity and μ is the dynamic viscosity. If the particle is free to rotate, its angular velocity is in the same direction as if it were rolling on the wall. Far-field analyses have been widely used to evaluate the motion of small particles or microswimmers near a boundary. More discussion on this topic can be found in the textbooks (Happel & Brenner 2012; Kim & Karrila 2013). In the near-contact regime, lubrication theory is utilized to analyse the flow within the thin fluid film between the particle and the wall (O'Neill & Stewartson 1967; Jeffrey 1982). The drag force on a sphere moving perpendicular to the wall increases as the gap distance decreases, following $F \sim a/(h - a)$. If the sphere is moving parallel to the wall, the force increases as $F \sim \ln(h/a - 1)$.

At arbitrary separation distances, numerical simulations are conducted to study the hydrodynamics of particle motion. For axisymmetric problems, such as a sphere translating or rotating perpendicular to a planar or a spherical wall in a quiescent viscous fluid, exact solutions represented by bipolar coordinate variables have been calculated by Jeffery (1915), Stimson & Jeffery (1926) and Brenner (1961). For non-axisymmetric cases, solutions for a sphere's translation and rotation parallel to a plane wall were derived by Dean & O'Neill (1963), O'Neill (1964) and Goldman, Cox & Brenner (1967). Ganatos, Weinbaum & Pfeffer (1980*b*) and Ganatos, Pfeffer & Weinbaum (1980*a*) studied the motion of a sphere between two parallel plane walls using the boundary collocation method. Their results demonstrated reasonable agreement between the far-field

approximation and the exact results when the sphere is located a few radii away from both walls. However, the far-field analysis becomes inaccurate as the separation distance decreases, and it may incorrectly predict the direction of the torque.

When the wall is non-planar, the particle motion may differ significantly from that near a plane wall. The surface roughness can eliminate the singularity in the lubrication force and enables the sphere to collide with the wall under pure hydrodynamic effects. Lecoq *et al.* (2004) measured the velocity of a sphere settling towards a corrugated wall which consists of parallel periodic wedges with small amplitude and wavelength compared with the particle size. Their results show that, at a large gap distance, the sphere motion is similar to that near a plane surface levelled in the middle between the peak and valley of the roughness. At a small distance, the sphere velocity is higher near a rough surface compared with its velocity near the virtual plane. Similar results are also found for spheres settling near surfaces of random arrays of pillars (Kunert, Harting & Vinogradova 2010; Chastel & Mongruel 2016). These studies have focused on the effects of small surface roughness on particle motion, while the influence of a curved wall with large amplitude has not been investigated. One significant effect is that a curved wall can cause additional cross-coupling terms in the mobility matrix. Consequently, a sphere may translate and rotate in the direction perpendicular to the applied force or torque. This mechanism presents a promising approach for particle separation based on their size or shape using micro-rough surfaces (Belyaev 2017) and serpentine microchannels (Di Carlo *et al.* 2007). However, a more comprehensive understanding of the underlying hydrodynamics is still required.

A curved wall also generates heterogeneous resistance to fluid flows along different directions. The surface corrugation is found to significantly modify the flow inside the viscous sublayer of streaming flows parallel or perpendicular to the wave direction, thereby reducing the flow drag at higher Reynolds numbers (Bechert & Bartenwerfer 1989; Luchini, Manzo & Pozzi 1991). At a certain distance away from the wall, the flows in both directions can essentially be viewed as uniform shear flows bounded by two virtual planes. The virtual plane for the flow perpendicular to the wave is located deeper into the fluid than the one for the parallel flow, therefore leading to larger resistance and changing the near-wall flow structures (Luchini *et al.* 1991). Pozrikidis (1987) studied the shear- and pressure-driven flow in channels of sinusoidal walls and found that surfaces with large wave amplitude can reverse the flow direction in the trough region, leading to the formation of Moffatt vortices (Moffatt 1964). The critical wave amplitude for vortex formation, as well as the dependence of eddy size on the wave amplitude, were also characterized. We expect that the particle motion near a curved surface will exhibit similar effects.

So far, studies on particle motion near non-planar walls are limited and they all rely on the assumption of small-amplitude surface corrugation. Based on a far-field analysis, Rad & Najafi (2010) analysed the influence of a small-amplitude sinusoidal surface on the sphere's translation mobility and the hydrodynamic interactions between two spheres. Their analysis shows that the sphere mobility decreases near a local hump and increases near a valley. However, their results are quantitatively inaccurate as they fail to correctly reproduce the solutions for a sphere moving near a plane surface in the limit of infinitely large wavelengths. Assoudi *et al.* (2018) studied the influence of wall roughness on the sphere motion in a shear flow and showed that the asymmetry of the roughness generates a lift force on the sphere and modifies its trajectory. Kurzthaler *et al.* (2020) showed that, when close to a randomly rough surface, the sphere moving parallel to the wall undergoes a translation perpendicular to the applied force. The random roughness, which causes a non-monotonic dependence of the variance of the sphere's mobility coefficients on the

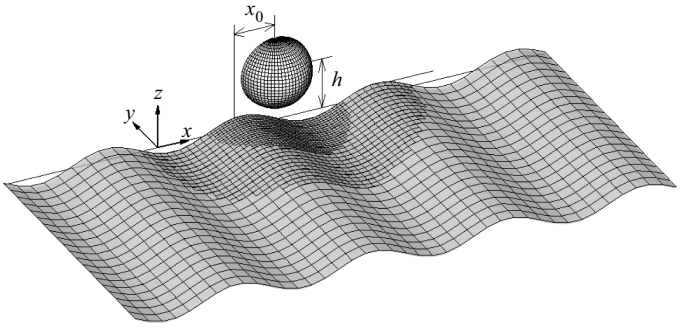

Figure 1. Schematic of the sphere moving near a sinusoidal surface. In the numerical simulation, half of the region is considered and the surface area is $200a \times 100a$ with a locally refined mesh in the gap between the surface and sphere.

surface characteristic wavelength, results in a complex spatial dependence of the particle diffusion rate under Brownian effects. The fluctuation of velocity along the force direction saturates at large wavelengths, while the transverse velocity and the velocity component perpendicular to the wall reach their maximum at a wavelength comparable to the sphere radius. All of these studies are based on the far-field approximation, the effects of the near-field hydrodynamic effects have not been considered yet.

Analysing the particle motion near a curved wall is also helpful in understanding the behaviour of microorganisms or active particles near complex surfaces. The first-order hydrodynamic effects of a sinusoidal surface on the swimming motion of a microswimmer was recently studied by Kurzthaler & Stone (2021) using point singularities to model the swimmer. Their study showed that, when the distance between the microswimmer and the surface is comparable to the surface wavelength, the reflection of flow fields at the edge of the valleys generates a repulsive force to decrease the wall attraction of the swimmer. Using a boundary element method, Ishimoto, Gaffney & Smith (2021) numerically studied the motion of a puller squirmer near small-amplitude sinusoidal surfaces. The squirmer is found to be stably attracted to the surface following an oscillating trajectory. The equilibrium height of the squirmer above the wall is largely influenced by the surface wavelength and the orientation of the swimmer. A local attraction of the squirmer towards the surface troughs is also observed. These results demonstrate the potential of utilizing surface topographies to provide directional guidance for self-swimming particles.

To understand the underlying Stokesian hydrodynamics, this work investigates the sphere motion near a sinusoidal surface and characterizes the effects of wavelength, amplitude and particle–wall distance on the sphere mobility. The rest of this paper is organized as follows. Section 2 presents the mathematical model of this problem. In § 3, sphere motions in the far-field and near-contact limits are analysed using the domain perturbation method and Lorentz reciprocal theorem. Section 4 discusses the results of a boundary element simulation of particle motion with arbitrary distance from a wall of large amplitude. Finally, the concluding remarks are presented in § 5.

2. Mathematical model

Figure 1 illustrates a spherical particle with radius a moving near a sinusoidal surface $z = A_{max} \cos kx$, where $k = 2\pi/\lambda$ is the wavenumber, and λ is the wavelength. The sphere is positioned at $\boldsymbol{r}_0 = (x_0, 0, h)$ and is subjected to a constant force $\boldsymbol{F}$ without any torque. The primary task of this work is to determine the dependence of sphere mobility on x_0

and h. The hydrodynamic interaction between the sphere and the wall is described by the incompressible Stokes equation

$$-\nabla \cdot \boldsymbol{\sigma} = 0, \quad \nabla \cdot \boldsymbol{u} = 0, \tag{2.1a}$$

where $\boldsymbol{\sigma} = p\boldsymbol{I} + \mu\nabla(\boldsymbol{u} + \boldsymbol{u}^{\mathrm{T}})$ is the fluid stress tensor, p is the pressure, $\boldsymbol{u}$ is the fluid velocity, $\boldsymbol{I}$ is the identity matrix and μ is the fluid viscosity. The boundary conditions for the fluid flow are

$$\boldsymbol{u} = \boldsymbol{U} + \boldsymbol{r} \times \boldsymbol{\Omega}, \quad \text{on } S_p, \tag{2.2a}$$

$$\boldsymbol{u} = \boldsymbol{0}, \quad \text{on } S_w \text{ and } S_\infty, \tag{2.2b}$$

where $\boldsymbol{U}$ and $\boldsymbol{\Omega}$ are the translational and rotational velocities of the sphere, S_p, S_w and S_∞ represent the sphere's surface, the curved wall and the bounding surface at infinity, respectively. The sphere velocity is determined by satisfying the force and torque balancing condition,

$$\int_{S_p} \boldsymbol{n} \cdot \boldsymbol{\sigma}\, \mathrm{d}S + \boldsymbol{F} = 0, \quad \int_{S_p} \boldsymbol{r} \times (\boldsymbol{n} \cdot \boldsymbol{\sigma})\, \mathrm{d}S = 0, \tag{2.3a,b}$$

where $\boldsymbol{n}$ denotes the unit normal vector pointing into the fluid on the sphere's surface. In the following sections, we will solve the above equations using theoretical and numerical methods for curved surfaces with small and arbitrary amplitudes, respectively.

3. Small-amplitude asymptotics

This section presents the theoretical analysis of a sphere's mobility matrix near a sinusoidal surface with small-amplitude fluctuations. The analysis follows the approach from Kurzthaler & Stone (2021), which used small-amplitude asymptotics and the Lorentz reciprocal theorem to solve for the roughness-induced velocity of a point swimmer. Considering a curved wall $z = A(x, y)$ with small amplitude compared with its wavelength, we introduce a small parameter $\varepsilon = A_{max}k \ll 1$, where $A_{max} = \max(|A(x, y)|)$ is the maximum absolute roughness of the surface. Applying the method of domain perturbation, the fluid velocity is expanded as

$$\boldsymbol{u} = \boldsymbol{u}^{(0)} + \varepsilon \boldsymbol{u}^{(1)} + O(\varepsilon^2), \tag{3.1}$$

where $\boldsymbol{u}^{(0)}$ and $\boldsymbol{u}^{(1)}$ are the $O(1)$ and $O(\varepsilon)$ fluid velocities. Substituting the above expansion into (2.1) and (2.2), the governing equations of each order remain as the Stokes equation, while the boundary condition on the curved surface S_w is expanded as

$$\boldsymbol{u}|_{z=A(x,y)} = \boldsymbol{u}^{(0)}|_{z=0} + \varepsilon \left(\boldsymbol{u}^{(1)} + Z(x, y)\frac{\partial \boldsymbol{u}^{(0)}}{\partial z} \right)\bigg|_{z=0} + O(\varepsilon^2), \tag{3.2}$$

where $Z(x, y) = A(x, y)/(A_{max}k)$ is the rescaled surface height. The right-hand side of the above equation corresponds to the $O(1)$ and $O(\varepsilon)$ boundary conditions, which respectively represent a no-slip condition at the plane wall and a slip velocity condition at $z = 0$ due to the surface corrugation. One can then solve the governing equation of each order with the corresponding boundary conditions. The zeroth-order solution $\boldsymbol{u}^{(0)}$, which describes the sphere motion near a plane wall, can be found in the literature using methods of bipolar harmonics or near-contact/far-field asymptotic analyses (O'Neill 1964; Goldman *et al.* 1967; O'Neill & Stewartson 1967; Happel & Brenner 2012). On the other hand, the first-order velocity $\boldsymbol{u}^{(1)}$, which represents the velocity induced by the surface roughness,

does not require explicit solution. Instead, we can apply the reciprocal theorem to the $\boldsymbol{u}^{(0)}$ field to directly find the sphere mobility. The reciprocal theorem has been widely used in the studies of the motion of inert and active particles under the influence of surface confinement, non-Newtonian fluids and external forces (Stone & Samuel 1996; Elfring 2017; Li & Koch 2020). A comprehensive review of its diverse applications in fluid dynamics can be found in Masoud & Stone (2019).

To utilize the Lorentz reciprocal theorem, we need to set up an auxiliary problem with known solutions. For our purpose, the auxiliary problem represents the flow field caused by an externally driven, translating or rotating sphere with the same distance h away from a plane wall. Its solution corresponds to the $\boldsymbol{u}^{(0)}$ velocity field as the original problem. The sphere velocities $\boldsymbol{U}^{(1)}$ and $\boldsymbol{\Omega}^{(1)}$ are connected to the auxiliary problem as follows:

$$\hat{\boldsymbol{F}} \cdot \boldsymbol{U}^{(1)} + \hat{\boldsymbol{T}} \cdot \boldsymbol{\Omega}^{(1)} = \int_{z=0} Z(x, y) \left((\boldsymbol{n} \cdot \hat{\boldsymbol{\sigma}}) \cdot \frac{\partial \boldsymbol{u}^{(0)}}{\partial z} \right) \Bigg|_{z=0} \mathrm{d}S, \tag{3.3}$$

where the symbol $\hat{}$ represents the auxiliary problem, $\hat{\boldsymbol{F}}$ and $\hat{\boldsymbol{T}}$ are the force and torque exerted on the particle. Note that the integration is performed on the plane wall at $z = 0$. This equation is valid for arbitrary surface topography and particle–wall distance as long as the surface fluctuation is small.

The translational and rotational velocities of the sphere are related to the force $\boldsymbol{F}$ and torque $\boldsymbol{\Omega}$ by a symmetric positive–definite mobility matrix $\boldsymbol{M}$

$$\begin{pmatrix} \boldsymbol{U} \\ \boldsymbol{\Omega} \end{pmatrix} = \boldsymbol{M} \cdot \begin{pmatrix} \boldsymbol{F} \\ \boldsymbol{T} \end{pmatrix}, \tag{3.4}$$

where $\boldsymbol{U} = (U_x, U_y, U_z)^{\mathrm{T}}$, and similarly for $\boldsymbol{\Omega}$, $\boldsymbol{F}$ and $\boldsymbol{T}$. The mobility matrix of a sphere near a corrugated wall with a small amplitude is expanded as

$$\boldsymbol{M} = \boldsymbol{M}^{(0)} + \varepsilon \boldsymbol{M}^{(1)}. \tag{3.5}$$

In the following, the mobility matrix of a sphere under both far-field and near-contact conditions will be analysed separately.

The leading-order mobility matrix $\boldsymbol{M}^{(0)}$ accounts for the hydrodynamic interaction between a sphere and a plane wall

$$\boldsymbol{M}^{(0)} = \begin{pmatrix} M_{11}^{(0)} & \cdot & \cdot & \cdot & M_{15}^{(0)} & \cdot \\ \cdot & M_{22}^{(0)} & \cdot & M_{24}^{(0)} & \cdot & \cdot \\ \cdot & \cdot & M_{33}^{(0)} & \cdot & \cdot & \cdot \\ \cdot & M_{24}^{(0)} & \cdot & M_{44}^{(0)} & \cdot & \cdot \\ M_{15}^{(0)} & \cdot & \cdot & \cdot & M_{55}^{(0)} & \cdot \\ \cdot & \cdot & \cdot & \cdot & \cdot & M_{66}^{(0)} \end{pmatrix}, \tag{3.6}$$

where the dots represent the identically zero terms because of the symmetry of the sphere-plane configuration.

When the sphere is far away from the wall, i.e. $a/h \ll 1$, its mobility factors are

$$\left.\begin{gathered} M_{11}^{(0)} = M_{22}^{(0)} \simeq \frac{1}{6\pi\mu a}\left(1-\frac{9a}{16h}\right), \quad M_{33}^{(0)} \simeq \frac{1}{6\pi\mu a}\left(1-\frac{9a}{8h}\right), \\ M_{44}^{(0)} = M_{55}^{(0)} \simeq \frac{1}{8\pi\mu a^3}\left(1-\frac{5}{16}\left(\frac{a}{h}\right)^3\right), \quad M_{66}^{(0)} \simeq \frac{1}{8\pi\mu a^3}\left(1-\frac{1}{8}\left(\frac{a}{h}\right)^3\right), \\ M_{15}^{(0)} = -M_{24}^{(0)} \simeq \frac{1}{64\pi\mu a^2}\left(\frac{a}{h}\right)^4\left(1-\frac{15a}{16h}\right). \end{gathered}\right\} \tag{3.7}$$

When the sphere is in near contact with the wall, i.e. $\delta = (h-a-A(x,y))/a \ll 1$, the mobility factors are

$$\left.\begin{gathered} M_{11}^{(0)} = M_{22}^{(0)} \simeq \frac{1}{6\pi\mu a}\left(-\frac{2}{\ln\delta}-\frac{4.4678}{(\ln\delta)^2}\right), \quad M_{33}^{(0)} \simeq \frac{1}{6\pi\mu a}\left(\delta+\frac{1}{5}\delta^2\ln\delta\right), \\ M_{44}^{(0)} = M_{55}^{(0)} \simeq \frac{1}{8\pi\mu a^3}\left(-\frac{8}{3\ln\delta}-\frac{3.7077}{(\ln\delta)^2}\right), \quad M_{66}^{(0)} \simeq \frac{1}{8\pi\mu a^3}\frac{1}{\zeta(3)}, \\ M_{15}^{(0)} = -M_{24}^{(0)} \simeq \frac{1}{8\pi\mu a^2}\left(-\frac{2}{3\ln\delta}-\frac{3.3888}{(\ln\delta)^2}\right), \end{gathered}\right\} \tag{3.8}$$

where $\zeta(3) = \sum_{n=1}^{\infty} n^{-3} = 1.20205$. These results are scattered across numerous previous studies, which analysed sphere translation (Brenner 1961; Maude 1961) and rotation (Jeffery 1915; Brenner 1962) perpendicular to the wall at a far distance, sphere motion parallel to the wall at a far distance (Maude 1963) and the near-contact motion of a sphere parallel (Goldman *et al.* 1967; O'Neill & Stewartson 1967) and perpendicular (Cox & Brenner 1967; Cooley & O'Neill 1969) to the wall. A comprehensive summary of the resistance matrix for different gap distances between a sphere and a plane can be found in Falade & Brenner (1988). In (3.8), the convergence of the leading-order terms to zero is slow due to the logarithmic dependence on $1/\ln\delta$, and to enhance accuracy, next-order corrections are often included by numerically fitting the coefficients.

From the symmetry of the sphere-wall configuration, it is straightforward to find that the $\mathrm{O}(\varepsilon)$ mobility matrix should satisfy

$$\boldsymbol{M}^{(1)} = \begin{pmatrix} M_{11}^{(1)} & \cdot & M_{13}^{(1)} & \cdot & M_{15}^{(1)} & \cdot \\ \cdot & M_{22}^{(1)} & \cdot & M_{24}^{(1)} & \cdot & M_{26}^{(1)} \\ M_{31}^{(1)} & \cdot & M_{33}^{(1)} & \cdot & M_{35}^{(1)} & \cdot \\ \cdot & M_{42}^{(1)} & \cdot & M_{44}^{(1)} & \cdot & M_{46}^{(1)} \\ M_{51}^{(1)} & \cdot & M_{53}^{(1)} & \cdot & M_{55}^{(1)} & \cdot \\ \cdot & M_{62}^{(1)} & \cdot & M_{64}^{(1)} & \cdot & M_{66}^{(1)} \end{pmatrix}. \tag{3.9}$$

Each row in the matrix can be calculated by separately applying a force or torque along the x-, y- or z-directions in (3.3), the coefficient is found to be

$$M_{ij}^{(1)} = M_{ji}^{(1)} = \frac{1}{k}\int_{-\infty}^{\infty} m_{ij}^{(1)}\cos k(x+x_0)\,\mathrm{d}x, \tag{3.10}$$

where

$$m_{ij}^{(1)} = \int_{y=-\infty}^{\infty}\left(\hat{\sigma}_{jz}\frac{\partial u_i^{(0)}}{\partial z}\right)\bigg|_{z=0}\mathrm{d}y, \tag{3.11}$$

and $\hat{\sigma}_{jz}$ and $\partial u_i^{(0)}/\partial z$ represent the hydrodynamic stresses and velocity gradients at $z = 0$. The subscripts $i, j = 1, 2, 3$ correspond to the cases where the sphere motion is driven by a force along the x-, y- and z-directions, respectively. For $i, j = 4, 5, 6$, the solution represents the sphere motion driven by a torque. The detailed derivation of each coefficient is provided in Appendix A. Equation (3.10) indicates that the influence of a small-amplitude curved surface on particle mobility is simply a linear combination of individual surface areas.

In the far-field approximation, the fluid velocity can be simplified as being generated by a Stokeslet. The coefficients in the above equation are

$$\left.\begin{gathered} m_{11}^{(1)} = -\frac{45}{\Delta}h^2x^2(8x^2+h^2), \quad m_{22}^{(1)} = -\frac{9}{\Delta}h^2(x^2+h^2)(8x^2+3h^2), \\ m_{33}^{(1)} = -\frac{45}{\Delta}h^4(8x^2+h^2), \quad m_{44}^{(1)} = -\frac{9}{4\Delta}(8x^4+x^2h^2+28h^4), \\ m_{55}^{(1)} = -\frac{45}{4\Delta}(8x^4-13x^2h^2+7h^4), \quad m_{66}^{(1)} = -\frac{45}{4\Delta}h^2(8x^2+h^2), \\ m_{13}^{(1)} = \frac{45}{\Delta}h^3x(8x^2+h^2), \quad m_{15}^{(1)} = -\frac{45}{\Delta}hx^2(4x^2-3h^2), \\ m_{24}^{(1)} = \frac{9}{\Delta}h(x^2+h^2)(4x^2-h^2), \quad m_{26}^{(1)} = 0, \\ m_{35}^{(1)} = \frac{45}{\Delta}h^2x(4x^2-3h^2), \quad m_{46}^{(1)} = -\frac{315}{4\Delta}h^3x, \end{gathered}\right\} \tag{3.12}$$

where $\Delta = 512\pi\mu(x^2+h^2)^{9/2}$. If we further assume that the distance between the sphere and the wall is small compared with the wavelength, i.e. $kh \ll 1$, the mobility factors can be explicitly solved as

$$\left.\begin{gathered} M_{11}^{(1)} = \frac{3a(-8+9h^2k^2)C_k}{256h^2\pi\mu}, \quad M_{22}^{(1)} = \frac{3a(-8+3h^2k^2)C_k}{256h^2\pi\mu}, \\ M_{33}^{(1)} = \frac{3a(-4+h^2k^2)C_k}{64h^2\pi\mu}, \quad M_{44}^{(1)} = \frac{15a(-8+h^2k^2)C_k}{1024\pi\mu h^4}, \\ M_{55}^{(1)} = \frac{3a(-40+7h^2k^2)C_k}{1024\pi\mu h^4}, \quad M_{66}^{(1)} = \frac{3a(-4+h^2k^2)C_k}{256\pi\mu h^4}, \\ M_{13}^{(1)} = -\frac{3akS_k}{32\pi\mu h}, \quad M_{15}^{(1)} = \frac{9ak^2C_k}{256\pi\mu h}, \quad M_{35}^{(1)} = 0, \\ M_{24}^{(1)} = -\frac{3ak^2C_k}{256\pi\mu h}, \quad M_{26}^{(1)} = 0, \quad M_{46}^{(1)} = \frac{3akS_k}{128\pi\mu h^3}, \end{gathered}\right\} \tag{3.13}$$

where $C_k = \cos kx_0$ and $S_k = \sin kx_0$ are used for brevity. This result is valid for arbitrary wavelengths of the wall. The diagonal coefficients $M_{11}^{(1)}, M_{22}^{(1)}, \ldots, M_{66}^{(1)}$ consist of two terms in the numerators. The first term is caused by the variation in distance between the sphere and the wall, while the second term is attributed to wall curvature. This result is consistent with Falade & Brenner (1988), where the resistance coefficients of a sphere near a curved wall were derived under the assumption of small wall curvature, i.e. $A_{max}hk^2 \ll 1$ for a sinusoidal surface. For the cross-coupling terms, the ones with $k^2\cos kx_0$ indicate the effects caused by the wall curvature, while the terms with $k\sin kx_0$ denote the effects due

to the surface slope. Falade & Brenner (1988) derived $M^{(1)}_{13} = M^{(1)}_{46} = 0$ and cannot predict the transverse migration and rotation of a sphere induced by a curved wall.

In the near-contact limit, $\delta = (h - a - A(x, y))/a \ll 1$, solving the motion of a sphere near a curved wall with arbitrary wavelength is challenging because the sphere may collide with multiple points on the surface simultaneously. To avoid this situation, we focus on the cases where the surface has a small curvature $A_{max}hk^2 \ll 1$, similar to the work of Falade & Brenner (1988). The lubrication-theory solutions for a sphere moving close to a flat plane (Cox & Brenner 1967; Goldman *et al.* 1967; O'Neill & Stewartson 1967; Cooley & O'Neill 1969) can be employed to solve the $O(\varepsilon)$ mobilities by (3.3). However, to simplify the calculation, here, we utilize the solution of Falade & Brenner (1988) and calculate the mobility matrix by directly inverting the resistance matrix, $\boldsymbol{M} = \boldsymbol{R}^{-1}$. The $O(\varepsilon)$ mobility coefficients are

$$\left.\begin{gathered}
M^{(1)}_{11} = \frac{ak^2C_k}{6\pi\mu}\left(-\frac{201}{50\ln\delta} - \frac{3.02001}{(\ln\delta)^2}\right), \quad M^{(1)}_{22} = \frac{ak^2C_k}{6\pi\mu}\left(-\frac{99}{50\ln\delta} - \frac{13.5478}{(\ln\delta)^2}\right), \\
M^{(1)}_{33} = \frac{ak^2C_k}{6\pi\mu}\left(\delta + 0.2001\delta^{3/2}\right), \quad M^{(1)}_{44} = \frac{k^2C_k}{8\pi\mu a}\left(-\frac{66}{25\ln\delta} - \frac{17.1254}{(\ln\delta)^2}\right), \\
M^{(1)}_{55} = \frac{k^2C_k}{8\pi\mu a}\left(-\frac{34}{25\ln\delta} - \frac{5.66758}{(\ln\delta)^2}\right), \quad M^{(1)}_{66} = \frac{0.124286k^2C_k}{8\pi\mu a}, \\
M^{(1)}_{15} = \frac{k^2C_k}{8\pi\mu}\left(-\frac{41}{25\ln\delta} - \frac{5.22177}{(\ln\delta)^2}\right), \quad M^{(1)}_{24} = \frac{k^2C_k}{8\pi\mu}\left(\frac{59}{25\ln\delta} + \frac{17.6088}{(\ln\delta)^2}\right).
\end{gathered}\right\} \tag{3.14}$$

These terms represent the first-order contribution of the wall curvature $\sim k^2\cos kx_0$ to the sphere motion due to the lubrication effects. Detailed information regarding $\boldsymbol{R}$ for a sphere near a wall with small curvature, as well as the derivation of $\boldsymbol{M}$, is provided in Appendix B.

Figure 2 shows the effects of the surface wavelength on the particle mobility near a sinusoidal surface under far-field hydrodynamic interaction. The results are normalized by the sphere's mobility $M_0 = 1/(6\pi\mu a)$ (or M_0/a for the cross-coupling terms) in an unbounded fluid. The three rows, from top to bottom, represent the translational and angular velocities of the sphere driven by a force in the x-, y- and z-directions, respectively. For $\lambda/h \ll 1$, the effects of the surface roughness smear out and all $O(\varepsilon)$ velocities reduce to zero. For $\lambda/h \gg 1$, the sphere moves near a local flat plane at a new distance $h - \varepsilon\cos kx_0$, thereby $U^{(1)}_x \simeq -9a\cos kx_0/16h^2$, $U^{(1)}_z$ and $\Omega^{(1)}_y$ approach zero. At intermediate wavelengths, the surface roughness generates a non-trivial impact on particle motion, even when considering only the far-field hydrodynamics. In figure 2(a), the local hill/valley of the wave tends to decrease/increase the horizontal velocity of the particle for $\lambda/h < 0.9352$ and $\lambda/h > 4.3192$, while, at an intermediate wavelength, the surface wave causes the opposite effects. Similar behaviour is also observed for roughness-induced particle rotation in figure 2(c). At the leading order, the sphere rotates in a direction as if it were rolling on the wall. The surface roughness with a large wavelength ($\lambda/h > 1.8405$) tends to enhance/impede the particle rotation by decreasing/increasing the effective distance. While at a small wavelength, the trend is the opposite. This is because the edges of the surface valley cause a reflection of the flow field and change the flow direction (Pozrikidis 1987). Figure 2(b) shows the leading-order vertical migration velocity $U^{(1)}_z$ since $U^{(0)}_z = 0$. At $0 \le x_0/\lambda \le 0.5$, $U^{(1)}_z$ is always negative for $\lambda/h > 1.2082$ and positive for $\lambda/h < 1.2082$, suggesting that the particle trajectory may follow the same or opposite

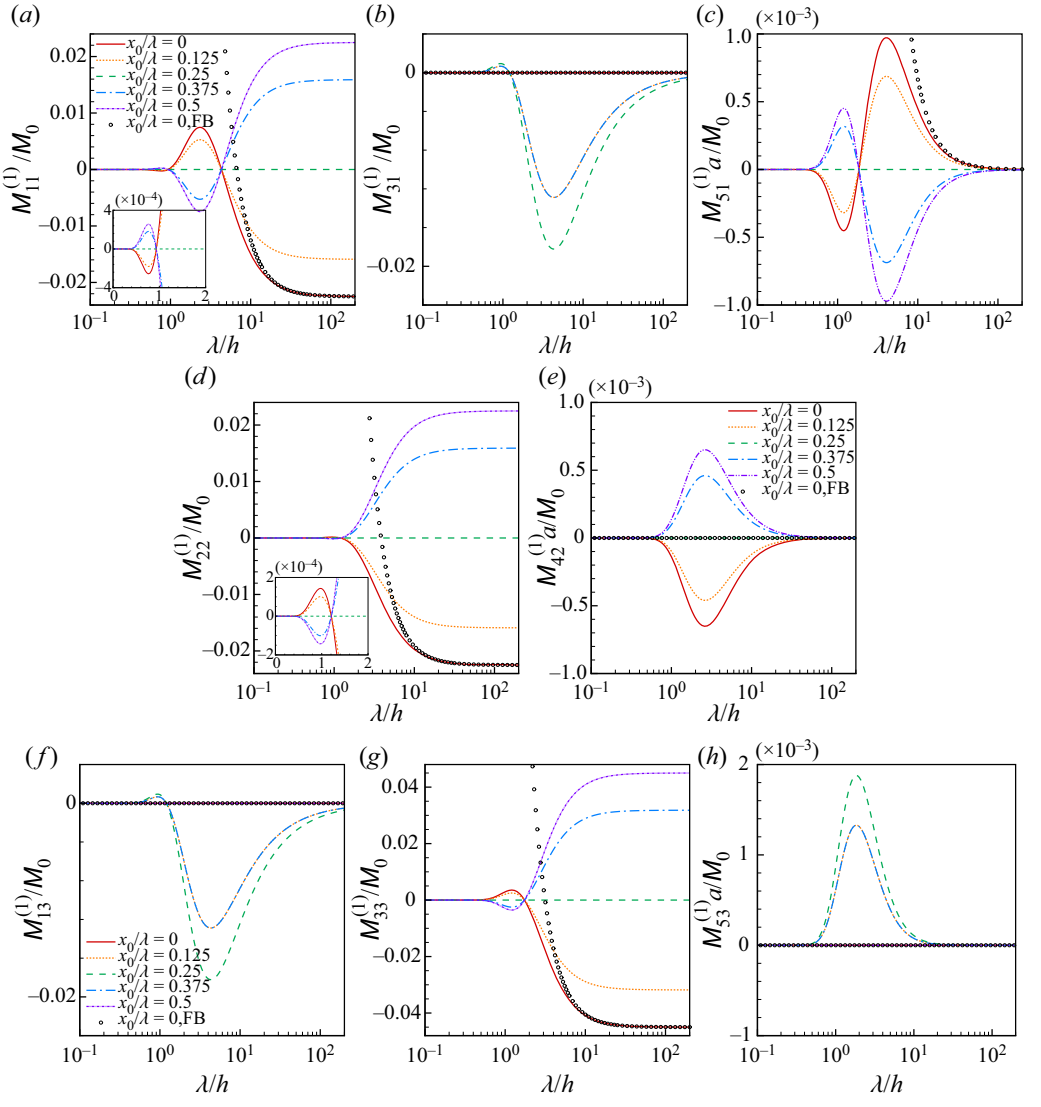

Figure 2. Normalized $O(\varepsilon)$ mobility coefficients of a sphere at different distances away from a sinusoidal surface; $M_0 = 1/(6\pi\mu a)$ is the sphere's translational mobility in an unbounded fluid. Symbols represent the results of Falade & Brenner (1988) for $x_0/\lambda = 0$.

phase of the sinusoidal wave, depending on the surface wavelength. This non-monotonic dependence of sphere mobility on the surface wavelength, which is not captured by the solution of Falade & Brenner (1988), has potential applications for separating small particles and cells using surfaces with designed topography. It is important to note that the distance h only affects the magnitude of the $O(\varepsilon)$ mobility, but does not change the critical value of λ/h at which the $O(\varepsilon)$ mobility changes sign.

Figures 2(*d*) and 2(*e*) show the particle mobility under a force transverse to the wave direction. Because of the symmetry of the sphere-surface configuration, the particle motion along the grooves of the sinusoidal wall cannot produce a velocity perpendicular to the wall. For $\lambda/h \ll 1$ or $\lambda/h \gg 1$, the sinusoidal surface approaches a flat plane and

the sphere velocity is isotropic inside the plane parallel to the wall. The particle velocity decreases/increases near the hill/valley of the surface for $\lambda/h > 1.2082$, and this effect is reversed for $\lambda/h < 1.2082$ with a much weaker influence. This result is different from $U_x^{(1)}$, highlighting the anisotropy of the in-plane mobility of a sphere near a sinusoidal surface with an intermediate wavelength. For $\Omega_x^{(1)}$, its direction is independent of the wavelength. The angular velocity is always enhanced/reduced as the surface roughness decreases/increases the gap distance, which differs from the $\Omega_y^{(1)}$ in figure 2(*c*). In the far-field analysis, $\Omega_z^{(1)}$ is predicted to be zero. However, as we will see later, this is not true when the higher-order hydrodynamic effects are considered.

The third row shows the sphere mobility driven by a force perpendicular to the wall. Figure 2(*f*) is identical to figure 2(*b*) due to the symmetry of the mobility matrix. For $\lambda/h > 1.2082$, the particle is horizontally attracted to the hill of the wave, while for $\lambda/h < 1.2082$, it is attracted to the valley. In figure 2(*g*), the vertical motion of the particle is enhanced/impeded when the gap distance is increased/decreased by the surface roughness of $\lambda/h > 1.7416$. The particle velocity approaches $U_z^{(1)} \simeq -9\cos kx_0/8h^2$ as the wavelength increases. For $\lambda/h < 1.7416$, the direction of $U_z^{(1)}$ is reversed. Figure 2(*h*) shows that the angular velocity $\Omega_y^{(1)}$ is always positive, meaning that the far-field effect drives the particle to rotate in the opposite direction compared with the rolling-type rotation of a sphere settling in parallel to a vertical wall. This effect is not predicted by the small-curvature analysis (Falade & Brenner 1988).

To further explain the non-monotonic dependence of particle mobility on the wavelength, figure 3 compares the $O(\varepsilon)$ mobility contribution of different segments of the sinusoidal surface. Here, we focus on the translational movement. The mobility contribution of each surface segment is determined by integrating (3.10) over the corresponding range of x. The sphere is positioned at $x_0 = 3\lambda/8$ and $h = 5a$, and the surface is divided into a series of inclined surfaces by half of the wavelength. At a small corrugation amplitude, each surface segment independently affects the particle motion. As expected, the surface segments closest to the sphere have the largest impact on particle mobility. The O(ε) mobility due to the entire sinusoidal surface can be effectively approximated by considering only the first three segments closest to the sphere. This approximation becomes less accurate at $\lambda \sim h$. At a large wavelength, the inclined surface S_1 directly below the sphere dominates the corrugation-induced mobility. It enhances the diagonal translation mobility by increasing the sphere-surface distance. At intermediate wavelengths, it generates a negative $M_{11}^{(1)}$ and reduces the sphere mobility in the x-direction. It indicates that the sphere mobility is influenced by both the sphere–wall gap distance and the angle of the inclined surface, which determines the relative importance of the anisotropic mobilities perpendicular and parallel to the surface. In comparison, the surface S_1 induces a positive–definite $M_{22}^{(1)}$ at all wavelengths, showing that the transverse motion is primarily influenced by the increased gap distance. The surface S_2 further increases $M_{22}^{(1)}$ due to the increase of the equivalent gap distance from the sphere. For the off-diagonal component, the surface S_1 induces a negative–definite $M_{13}^{(1)}$. At intermediate wavelengths, $M_{13}^{(1)}$ becomes positive mainly due to the influences of S_2.

The above results are in qualitative agreement with the previous analysis of the far-field interaction of a microswimmer with a corrugated surface (Kurzthaler *et al.* 2020). Their study provides the corrugation-induced velocities for higher-order singularities, including force dipole, source dipole, force quadrupole and rotlet dipole, which also show non-monotonic variation with the wavelength. However, limited by the small-amplitude

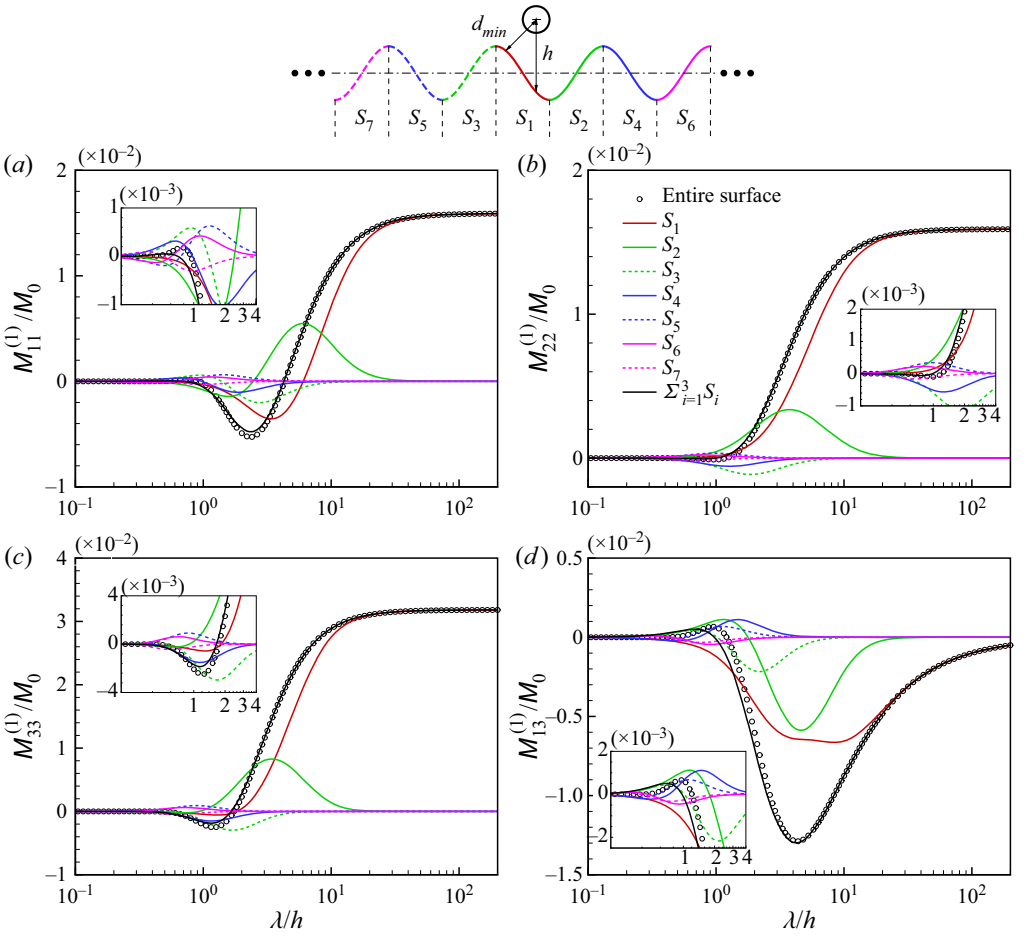

Figure 3. The contribution of different surface segments on the sphere's $O(\varepsilon)$ translational mobility coefficients, $x_0 = 3\lambda/8$ and $h = 5a$.

approximation, surface corrugation has weak effects on particle mobility. In the next section, numerical simulations will be performed to study the sphere motion near a large-amplitude surface and stronger effects from the surface corrugation will be observed.

4. Numerical simulation

In this section, the Stokes equation is numerically solved for a sphere moving near a sinusoidal surface using an in-house developed boundary element code. The approach is based on the previous work by Pozrikidis (2002) and Zhu, Lauga & Brandt (2013). Both the sphere and the sinusoidal wall are modelled as rigid solid bodies. The fluid velocity around rigid bodies in an unbounded fluid domain can be represented in the following integral form:

$$\boldsymbol{u}(\boldsymbol{r}) = \frac{1}{8\pi\mu} \int_{S_p+S_w} \boldsymbol{G}(\boldsymbol{r}-\boldsymbol{r}') \cdot \boldsymbol{f}(\boldsymbol{r}')\, \mathrm{d}S', \tag{4.1}$$

where $\boldsymbol{G} = \boldsymbol{I}/r + \boldsymbol{r}\boldsymbol{r}/r^3$ is the Green's function for the Stokes flow, $\boldsymbol{I}$ is the Kronecker delta tensor, $r = \sqrt{\boldsymbol{r}\cdot\boldsymbol{r}}$ is the distance and $\boldsymbol{f}$ is the unknown force acting on the fluid by the

discretized surface element. Due to the symmetry of the problem, the current simulation considers only half of the domain ($y \leq 0$). The halves of the sphere and surface are discretized using N_s and N_w quadrilateral elements, respectively. On each surface element S_i, the unknown element force $\boldsymbol{f}_i$ is assumed to be constant and contributes to the velocity of the solid body by

$$\boldsymbol{u}_j = \frac{1}{8\pi\mu} \sum_{i=1}^{N_s+N_w} \boldsymbol{f}_i \int_{S_i} \boldsymbol{G}(\boldsymbol{r}_j - \boldsymbol{r}_i)\, \mathrm{d}S, \tag{4.2}$$

and leads to $3(N_s + N_w)$ independent linear equations. For the elements on the wall surface, the velocity $\boldsymbol{u}_j$ is fixed to zero, and for the sphere elements, the velocity is determined by the rigid body motion

$$\boldsymbol{u}_i = \boldsymbol{U} + \boldsymbol{\Omega} \times (\boldsymbol{r}_i - \boldsymbol{r}_0), \tag{4.3}$$

where $\boldsymbol{U}$ and $\boldsymbol{\Omega}$ are the unknown translational and rotational velocities, and $\boldsymbol{r}_0$ is the centre of the sphere. The linear system is then closed by 6 extra linear equations satisfying the force and torque balance of the sphere

$$\sum_{i=1}^{N_s} \boldsymbol{f}_i = \boldsymbol{F}, \quad \sum_{i=1}^{N_s} (\boldsymbol{r}_i - \boldsymbol{r}_0) \times \boldsymbol{f}_i = \boldsymbol{T}, \tag{4.4a,b}$$

where $\boldsymbol{F}$ and $\boldsymbol{T}$ are the external force and torque applied on the sphere. As the sphere is free of torque, $\boldsymbol{T}$ is set to zero in this study. The $(3N_s + 3N_w + 6) \times (3N_s + 3N_w + 6)$ matrix problem is solved for $\boldsymbol{f}_i$, $\boldsymbol{U}$ and $\boldsymbol{\Omega}$ using the DGESV function in LAPACK linear algebra library.

To validate the numerical code, the translation of a sphere near a plane wall is first simulated. The analytical and numerical solutions for the drag and torque coefficients of a sphere translating perpendicular or parallel to a plane wall can be found in Goldman *et al.* (1967). Quadrilateral elements are used to discretize both the sphere and the surface. Compared with triangular elements, such a method allows a natural parametrization of the edge to facilitate the numerical integration using the Gauss–Legendre quadrature. For singular elements, the simulation is transformed into an integration based on the plane polar coordinate system (Pozrikidis 2002). In this work, the half-sphere and the half-plane are discretized by 3100 and 16 022 elements, respectively. The grids are locally refined in the gap between the sphere and the wall, with the minimum grid $\sim 0.008a$. The size of the wall plane is $40a \times 40a$ following Zhu *et al.* (2013). The force and torque coefficients for a sphere moving perpendicular and parallel to the wall are compared against the literature, as shown in table 1. It is verified that the current simulation can accurately replicate the reported results.

For a sphere moving near a sinusoidal wall, a larger surface of $200a \times 100a$ is used to accurately capture the hydrodynamic effects of surface corrugation on the sphere motion. The sphere is located above the centre of the surface to minimize the error due to the truncation of the domain. As the sphere approaches the surface, the quadrilateral elements are successively refined by dividing them evenly into four elements in the gap region, ensuring an accurate simulation of the particle motion in both the far field and near field of the sinusoidal wall.

Figure 4 shows the normalized mobilities of the sphere near a sinusoidal surface of $A = 0.1a$. Consistent with previous findings by Spagnolie & Lauga (2012), the far-field approximation agrees reasonably well with the numerical results until $h \sim 2a$, after which the far-field analysis results show significant deviation and even show quantitative

	Perpendicular	Parallel	
h/a	Error, F_z(%)	Error, F_x(%)	Error, T_y(%)
3.7622	0.00731	0.00692	2.55353
2.3523	0.03911	0.01107	0.64911
1.5431	0.01377	0.01050	0.20855
1.1276	0.06249	0.00712	0.11724
1.0453	0.09800	0.01820	0.18547
1.005004	0.39652	0.24873	1.47696
1.003202	1.14405	0.16800	1.66146

Table 1. Comparison between the current simulation and the previous results for a sphere translating near an infinitely large rigid plane wall.

differences from the simulation. In the near-contact region, all the mobility components eventually reduce to zero as the gap distance decreases to zero. However, due to the $1/\ln\delta$ asymptotes, the sphere still has a relatively large velocity parallel to the wall even when it is in close proximity to the surface. For clarity, the $1/(\ln\delta)^2$ terms in the near-contact asymptotes are not shown here. The three diagonal components monotonically reduce to zero with decreasing h, while the off-diagonal terms initially reach a peak close to the wall and then decrease to zero. This trend is not captured by the far-field or lubrication asymptotes and requires extremely fine grid resolution to be fully captured in simulations.

In figures 4(a) and 4(d), the two mobilities M_{11} and M_{22} are close to each other because the particle motion is mainly influenced by the same virtual plane wall at $y = 0$. The sinusoidal wave affects their relative magnitudes at different horizontal locations (see insets). Figure 4(f) shows that the sphere has a non-zero Ω_z when it translates parallel to the grooves of the sinusoidal surface. This effect, which is mainly caused by the hydrodynamic interaction between the sphere and the locally inclined surface, is not captured by the far-field analysis at the leading order. In figure 4(h), the velocity $U_z \sim h$ linearly reduces to zero as the particle approaches the wall. The far-field analysis can predict the same trend, while the quantitative results are not correct. The vertical velocity U_z is significantly different from U_x and U_y. The anisotropic translational mobility of a particle perpendicular and parallel to the wall is a key factor for the accumulation of microswimmers near a surface (Berke *et al.* 2008; Li & Ardekani 2014). Similar behaviour can also be observed for microswimmers near a corrugated surface (Ishimoto *et al.* 2021; Kurzthaler & Stone 2021). Finally, in figure 4(i), the direction of the particle rotation is reversed when the particle–wall distance $h \lesssim 2a$, showing that the near-field hydrodynamic interaction causes the sphere to roll on the surface.

With a larger amplitude, the surface has stronger influences on the sphere mobility. Figure 5 shows the particle motion near a sinusoidal surface with $A = 5a$ and $\lambda = 20a$, for which the far-field analysis only qualitatively agrees with the numerical results. Here, for the far-field results, the sphere–wall distance h has subtracted the local surface height directly beneath the centre of the sphere. Surprisingly, this adjustment leads to a better agreement between the far-field and numerical results, especially for M_{51} and M_{42}. In figures 5(c) and 5(e), the translation-induced rotation at a large h is in the same direction as the sphere rolling on the surface. The result is the same as the sphere movement near a surface with a small amplitude. While, at an intermediate distance, the sphere will rotate in the opposite direction for $x_0 > \lambda/4$. This effect, which is caused by the strong hydrodynamic interaction between the sphere and a locally curved trough of the surface,

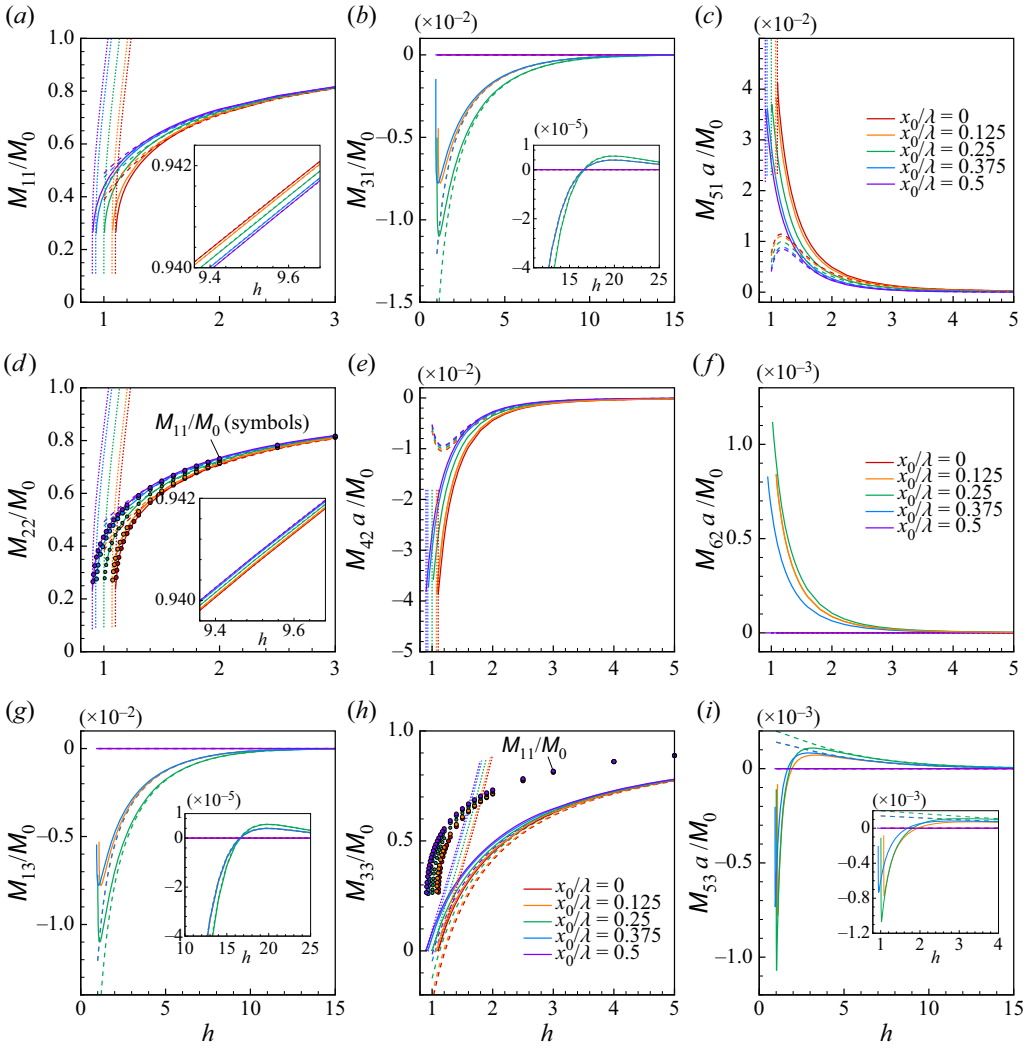

Figure 4. Normalized mobility coefficients of a sphere near a sinusoidal surface with $\lambda = 20a$ and $A = 0.1a$; $M_0 = 1/(6\pi\mu a)$ is the sphere's translational mobility in an unbounded fluid. Solid lines: numerical results, dashed lines: far-field solution, dotted lines: lubrication solution.

can be qualitatively captured by the far-field analysis. Further close to the surface, the particle returns to the rolling-type motion near the surface. Similar behaviour is also shown in figure 5(f), where Ω_z at $x = 3\lambda/4$ becomes negative at $0 \lesssim h \lesssim 5a$. In figure 5(g), the transverse velocity U_x of the sphere is negligible when it is far away from the surface and changes the direction at $h \simeq 21a$. When the sphere is close to the wall, the sinusoidal surface induces a large transverse velocity U_x of comparable magnitude to U_z. Since a sphere moving perpendicular to the wall requires a long time to collide with the wall, U_x can cause significant transverse migration of the particle along the wave direction. This effect leads to a strong accumulation of particles at the valley when they settle down towards a corrugated surface.

To better illustrate the sphere motion near a sinusoidal surface, figure 6 displays the trajectory of a sphere moving near a sinusoidal surface driven by a horizontal and

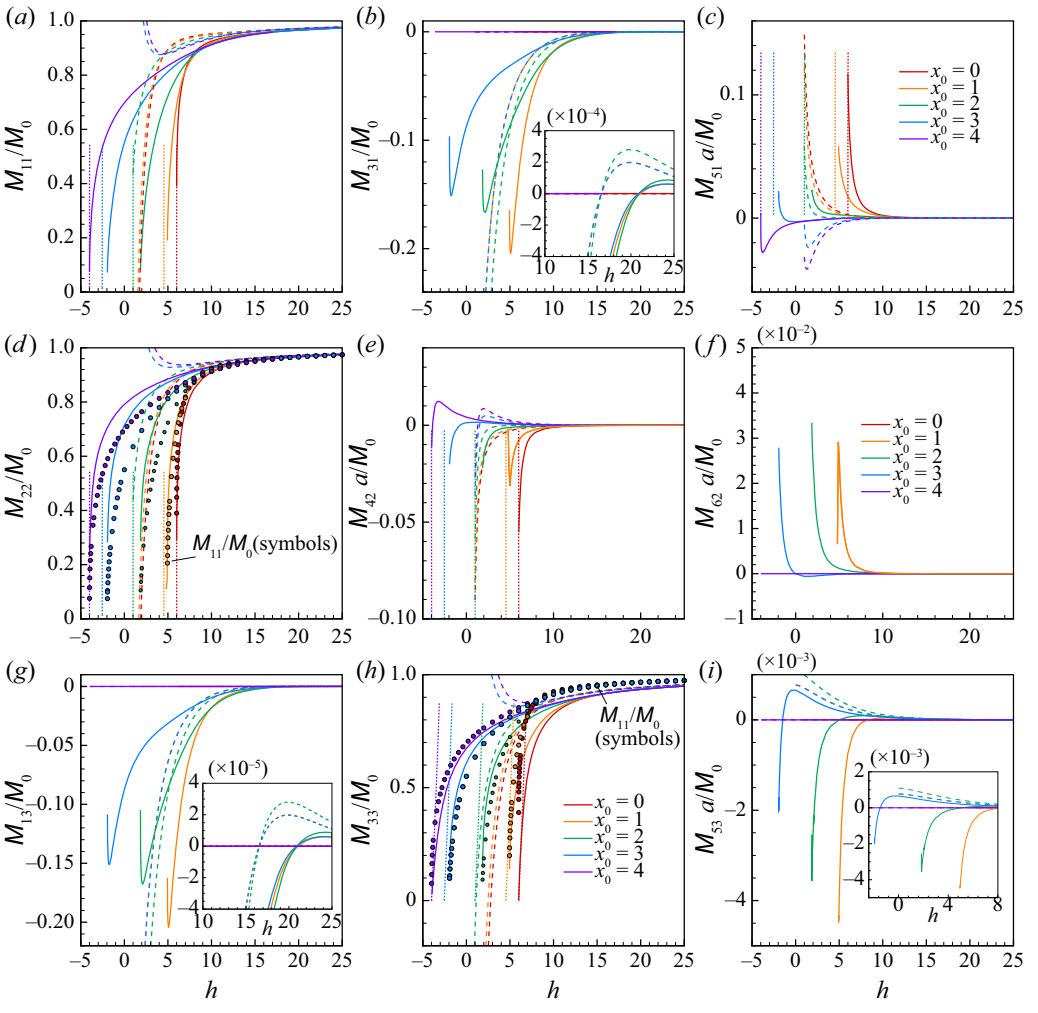

Figure 5. Normalized mobility coefficients of a sphere near a sinusoidal surface with $\lambda = 20a$ and $A = 5a$; $M_0 = 1/(6\pi\mu a)$ is the sphere's translational mobility in an unbounded fluid. Solid lines: numerical results, dashed lines: far-field solution, dotted lines: lubrication solution.

vertical force. The position of the sphere centre is explicitly updated over time using the fourth-order Adams–Bashforth scheme

$$\boldsymbol{r}_0^{n+1} = \boldsymbol{r}_0^n + \frac{\Delta t}{24}[55\boldsymbol{U}(\boldsymbol{r}_0^n) - 59\boldsymbol{U}(\boldsymbol{r}_0^{n-1}) + 37\boldsymbol{U}(\boldsymbol{r}_0^{n-2}) - 9\boldsymbol{U}(\boldsymbol{r}_0^{n-3})], \tag{4.5}$$

where the subscripts $n+1, n, n-1, \ldots$ represent different time steps and the step size is set to $\Delta t = 0.1$. Lower-order schemes are utilized for the initial time steps. To minimize simulation errors resulting from domain truncation, the sphere is positioned above the centre of the sinusoidal wall. At the $(n+1)$th time step, the discretized wall grids are updated using $z^{n+1} = A_{max}\cos k(x + x_0^n)$, where x_0^{n+1} is the new assigned x-location of the sphere centre. In figure 6(*a*), the sphere exhibits an oscillating trajectory when moving parallel to the surface. The trajectory is flattened when the sphere is moving above the valley of the surface, indicating a strong suppression of the vertical motion due to the

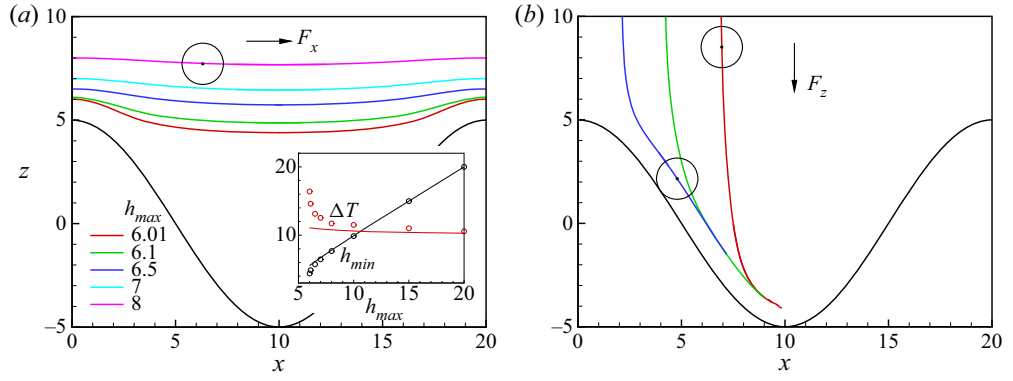

Figure 6. The trajectories of a sphere driven by a force (*a*) parallel and (*b*) perpendicular to a sinusoidal surface with $\lambda = 20a$ and $A = 5a$. The inset in (*a*) shows the dependence of the minimum height h_{min} of the sphere on the maximum height h_{max} and the travel time ΔT from $x_0 = 0$ to $x_0 = \lambda/2$, symbols show the numerical results and lines show the far-field approximate solution.

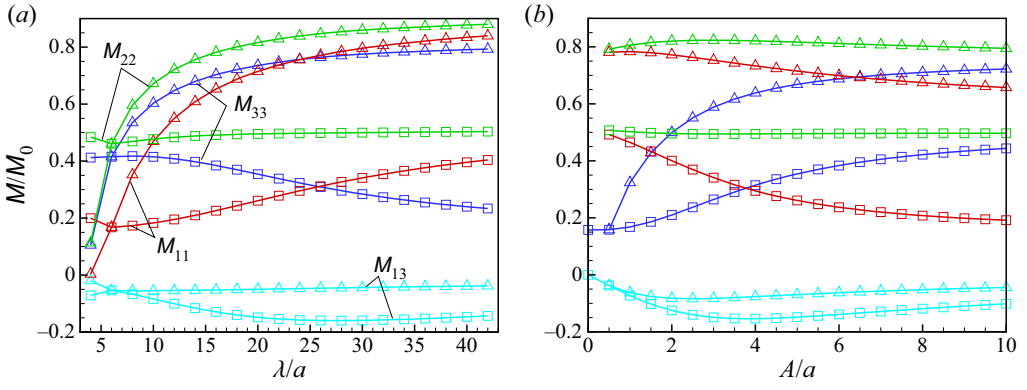

Figure 7. The translational mobility of a sphere at $x_0 = 3\lambda/8$ near a sinusoidal surface with (*a*) constant amplitude $A = 5a$ and varying wavelength, and (*b*) constant wavelength $\lambda = 20a$ and varying amplitude; $M_0 = 1/(6\pi\mu a)$ is the sphere's translational mobility in an unbounded fluid. Triangles represent the sphere has a fixed vertical position $h = 2.39627a$ and $h = 0.854141a$ in (*a*,*b*), respectively, and squares represent the sphere has a fixed minimum distance $d = 1.2a$ from the surface.

inclined walls on both sides. The amplitude of the oscillation increases as the trajectory is closer to the wall and, after one period, the sphere returns to the original height. In the inset of figure 6(*a*), the sphere close to the wall takes a much longer time to travel from $x_0 = 0$ to $x_0 = \lambda/2$. Figure 6(*b*) shows the trajectories of a sphere released from the same initial *y*-location $h = 10a$ and three different *x*-locations, $x/\lambda = 0.25, 0.5, 0.75$. The sphere descends towards the valley of the surface. This effect becomes stronger as the sphere approaches the surface. Eventually, the sphere is nearly in contact with the wall and falls along the surface.

Finally, we further compare the effects of surface wavelength and amplitude on the mobility of a sphere at a constant distance from the wall. Figure 7(*a*) shows the translational mobility of a sphere at $x_0 = 3\lambda/8$ near a surface with a constant amplitude $A = 5a$ and varying wavelengths. When the sphere is at a fixed height *h* (triangle symbols), all the diagonal mobilities increase monotonically with wavelength, and the off-diagonal mobility M_{13} reaches the minimum at $\lambda \simeq 6a$ and then slowly increases. The transverse

mobility M_{22} is always larger than the longitudinal and vertical mobilities, and the relative strength of M_{11} and M_{33} is dependent on the wavelength. For a sphere at constant gap distance from the surface (square symbols for $d_{min} = 1.2a$), M_{22} and M_{13} are weakly influenced by changing the wavelength, while M_{11} and M_{33} show stronger dependence on λ. Figure 7(b) shows qualitatively similar behaviour when changing the surface amplitude. These results demonstrate that the sphere's movement can become complicated by its near-field hydrodynamic interaction with a surface of large corrugation amplitude.

5. Conclusion

This work investigates the sphere mobility driven by an external force near a sinusoidal surface in the Stokes regime. For a surface with a small amplitude, solutions of far-field or near-contact approximation are derived using the Lorentz reciprocal theorem. At a large amplitude, the sphere mobility is solved using the boundary element method and shows good agreement with the two asymptotes. Compared with a plane surface, a corrugated surface induces additional translational and rotation velocity components to the particle's movement. The direction of the corrugation-induced velocities is dependent on the wavelength of the surface. The key finding is that, in the far-field regime, a sphere settling perpendicular to a sinusoidal surface tends to slowly migrate towards the hill of the wall while, in the near field, it migrates towards the valley with a large transverse velocity. As the sphere approaches the surface, the magnitude of the transverse velocity becomes comparable to the vertical velocity and can significantly affect the sedimentation process. At an intermediate distance from the wall, the far-field and lubrication theories fail to accurately calculate the sphere mobility, and numerical simulations are necessary to fully capture the hydrodynamics.

Acknowledgements. We would like to thank L. Zhu for the helpful discussion and the anonymous reviewers for their valuable comments in improving this manuscript.

Funding. This research is supported by the National Natural Science Foundation of China (No. 12102258, 12372264) and the Natural Science Foundation of Shanghai (No. 23ZR1430800).

Declaration of interests. The authors report no conflict of interest.

Author ORCIDs.
Gaojin Li https://orcid.org/0000-0001-7694-2430.

Appendix A. Derivation of the far-field mobility coefficients

When the particle is far away from the surface, the fluid flow can be characterized using the multipole expansion of the fundamental singularities of the Stokes equation. To simplify the expressions, the centre of the sphere is set to $\boldsymbol{r}_0 = 0\boldsymbol{e}_x + 0\boldsymbol{e}_y + h\boldsymbol{e}_z$, and the wall surface is written as $z = A_{max}\cos k(x + x_0)$. The force acting on the sphere is $\boldsymbol{F} = F(\cos\theta\boldsymbol{e}_\phi + \sin\theta\boldsymbol{e}_z)$, where F is the force magnitude, $\boldsymbol{e}_\phi = \boldsymbol{e}_x\cos\phi + \boldsymbol{e}_y\sin\phi$, θ is the angle between the z-axis and the force direction and ϕ is the angle between the x-axis and the force projection inside the $x - y$ plane. At the leading order, the velocity field is represented by a combination of a Stokeslet and the image singularities due to the plane wall

$$\boldsymbol{u}^{(0)}(\boldsymbol{r}) = \frac{F}{8\pi\mu}(\boldsymbol{G}(\boldsymbol{r} - \boldsymbol{r}_0, \boldsymbol{e}) + \boldsymbol{G}^*(\boldsymbol{r} - \boldsymbol{r}_0^*, \boldsymbol{e})). \tag{A1}$$

The first term represents the Stokeslet

$$\boldsymbol{G}(\boldsymbol{r},\boldsymbol{e})=\frac{1}{|\boldsymbol{r}|}\left(\boldsymbol{e}+\frac{(\boldsymbol{e}\cdot\boldsymbol{r})\boldsymbol{r}}{|\boldsymbol{r}|^2}\right), \tag{A2}$$

and the second term $\boldsymbol{G}^*$ represents the image singularities induced by a plane wall

$$\boldsymbol{G}^*(\boldsymbol{r}-\boldsymbol{r}_0^*,\boldsymbol{e})=-\boldsymbol{G}(\boldsymbol{e})+2h\boldsymbol{G}_D(\boldsymbol{e}^*,\boldsymbol{e}_z)-2h^2\boldsymbol{S}_D(\boldsymbol{e}^*), \tag{A3}$$

where $\boldsymbol{e}^*=\boldsymbol{e}_\phi\cos\theta-\boldsymbol{e}_z\sin\theta$, $\boldsymbol{r}_0^*=\boldsymbol{r}_0-2h\boldsymbol{e}_z$, and on the right-hand side we use a shorthand notation $\boldsymbol{G}(\boldsymbol{e})=\boldsymbol{G}(\boldsymbol{r}-\boldsymbol{r}_0^*,\boldsymbol{e})$. The three terms represent a Stokeslet, a Stokeslet dipole and a source dipole, respectively. The Stokeslet dipole and the source dipole are derivatives of a Stokeslet $\boldsymbol{G}_D(\boldsymbol{r}-\boldsymbol{r}_0,\boldsymbol{d},\boldsymbol{e})=\boldsymbol{d}\cdot\nabla_0\boldsymbol{G}(\boldsymbol{r}-\boldsymbol{r}_0,\boldsymbol{e})$ and $\boldsymbol{S}_D(\boldsymbol{r}-\boldsymbol{r}_0,\boldsymbol{e})=-\nabla_0^2\boldsymbol{G}(\boldsymbol{r}-\boldsymbol{r}_0,\boldsymbol{e})/2$, where ∇_0 represents gradient acting on the singularity position $\boldsymbol{r}_0$, and their expressions are

$$\boldsymbol{G}_D(\boldsymbol{r},\boldsymbol{d},\boldsymbol{e})=\frac{1}{|\boldsymbol{r}|^2}\left(\frac{(\boldsymbol{d}\cdot\boldsymbol{r})\boldsymbol{e}-(\boldsymbol{e}\cdot\boldsymbol{r})\boldsymbol{d}-(\boldsymbol{d}\cdot\boldsymbol{e})\boldsymbol{r}}{|\boldsymbol{r}|}+\frac{3(\boldsymbol{e}\cdot\boldsymbol{r})(\boldsymbol{d}\cdot\boldsymbol{r})\boldsymbol{r}}{|\boldsymbol{r}|^3}\right), \tag{A4}$$

$$\boldsymbol{S}_D(\boldsymbol{r},\boldsymbol{e})=\frac{1}{|\boldsymbol{r}|^3}\left(-\boldsymbol{e}+\frac{3(\boldsymbol{e}\cdot\boldsymbol{r})\boldsymbol{r}}{|\boldsymbol{r}|^2}\right). \tag{A5}$$

The pressure fields induced by a Stokeslet, a Stokeslet dipole and a source dipole are respectively

$$p_G=\frac{2\mu\boldsymbol{r}\cdot\boldsymbol{e}}{|\boldsymbol{r}|^3},\quad p_{GD}=\frac{2\mu}{|\boldsymbol{r}|^3}\left(\frac{3(\boldsymbol{r}\cdot\boldsymbol{e})(\boldsymbol{r}\cdot\boldsymbol{d})}{|\boldsymbol{r}|^2}-\boldsymbol{d}\cdot\boldsymbol{e}\right),\quad p_{SD}=0. \tag{A6a–c}$$

The pressure solution is used to calculate the hydrodynamic stresses for the auxiliary problem.

On the plane surface, the velocity gradients are

$$\left.\begin{aligned}\left.\frac{\partial u_x^{(0)}}{\partial z}\right|_{z=0}&=\frac{3xh(x\cos\theta\cos\phi+y\cos\theta\sin\phi-h\sin\theta)}{2\pi\mu(h^2+x^2+y^2)^{5/2}},\\ \left.\frac{\partial u_y^{(0)}}{\partial z}\right|_{z=0}&=\frac{3yh(x\cos\theta\cos\phi+y\cos\theta\sin\phi-h\sin\theta)}{2\pi\mu(h^2+x^2+y^2)^{5/2}},\end{aligned}\right\} \tag{A7}$$

and $\partial u_z^{(0)}/\partial z|_{z=0}=0$ by the incompressible condition.

To solve (3.3) using the reciprocal relation, two auxiliary problems are introduced to calculate the influence of the curved surface. The first problem describes a point force near a plane surface, which solution is shown above. The hydrodynamic stresses on the plane surface can be directly calculated as

$$\left.\begin{aligned}\hat{\sigma}_{xz}|_{z=0}=\mu\left.\frac{\partial u_x^{(0)}}{\partial z}\right|_{z=0},\quad \hat{\sigma}_{yz}|_{z=0}=\mu\left.\frac{\partial u_y^{(0)}}{\partial z}\right|_{z=0},\\ \hat{\sigma}_{zz}|_{z=0}=\frac{-3\mu h^2(x\cos\theta\cos\phi+y\cos\theta\sin\phi-h\sin\theta)}{2\pi(h^2+x^2+y^2)^{5/2}}.\end{aligned}\right\} \tag{A8}$$

Equations (A7) and (A8) are then substituted into (3.3) to derive the mobility coefficients of a sphere driven by a force near a non-planar surface.

The second auxiliary problem considers the sphere motion driven by a torque. In the leading order, the velocity is represented by a point torque near a plane

$$\boldsymbol{u}^{(0)}(\boldsymbol{r}) = \frac{T}{8\pi\mu}(\boldsymbol{R}(\boldsymbol{r}-\boldsymbol{r}_0,\boldsymbol{e}) + \boldsymbol{R}^*(\boldsymbol{r}-\boldsymbol{r}_0^*,\boldsymbol{e})), \tag{A9}$$

where the first term represents a rotlet

$$\boldsymbol{R}(\boldsymbol{r},\boldsymbol{e}) = \frac{\boldsymbol{e}\times\boldsymbol{r}}{|\boldsymbol{r}|^3}, \tag{A10}$$

and the second term represents the image singularities

$$\boldsymbol{R}^*(\boldsymbol{r}-\boldsymbol{r}_0^*,\boldsymbol{e}) = -\boldsymbol{R}(\boldsymbol{e}) + \cos\theta(-\boldsymbol{G}_D(\boldsymbol{e}_z,\boldsymbol{e}_\phi^\perp) - \boldsymbol{G}_D(\boldsymbol{e}_\phi^\perp,\boldsymbol{e}_z) + 2h\boldsymbol{S}_D(\boldsymbol{e}_\phi^\perp)), \tag{A11}$$

where $\boldsymbol{e}_\phi^\perp = \boldsymbol{e}_z\times\boldsymbol{e}_\phi$, $\boldsymbol{G}_D$ and $\boldsymbol{S}_D$ are the Stokeslet dipole and source dipole. The rotlet does not disturb the pressure field, i.e. $p_R = 0$.

On the plane surface, the velocity gradients are

$$\left.\begin{aligned}\left.\frac{\partial u_x^{(0)}}{\partial z}\right|_{z=0} &= -\frac{3h(xy\cos\theta\cos\phi + (h^2-x^2)\cos\theta\sin\phi + hy\sin\theta)}{4\pi\mu(h^2+x^2+y^2)^{5/2}},\\ \left.\frac{\partial u_y^{(0)}}{\partial z}\right|_{z=0} &= \frac{3h(xy\cos\theta\sin\phi + (h^2-y^2)\cos\theta\cos\phi + hx\sin\theta)}{4\pi\mu(h^2+x^2+y^2)^{5/2}},\end{aligned}\right\} \tag{A12}$$

and $\partial u_z^{(0)}/\partial z|_{z=0} = 0$ by the incompressible condition.

The hydrodynamic stresses on the plane surface induced by the rotlet is

$$\left.\begin{aligned}\hat{\sigma}_{xz}|_{z=0} = \mu\left.\frac{\partial u_x^{(0)}}{\partial z}\right|_{z=0}, \quad \hat{\sigma}_{yz}|_{z=0} = \mu\left.\frac{\partial u_y^{(0)}}{\partial z}\right|_{z=0},\\ \hat{\sigma}_{zz}|_{z=0} = \frac{3\mu h\cos\theta(y\cos\phi - x\sin\phi)}{2\pi(h^2+x^2+y^2)^{5/2}}.\end{aligned}\right\} \tag{A13}$$

For a surface $A(x,y) = A_{max}\cos k(x+x_0)$, the rescaled surface height $Z(x,y) = A(x,y)/(A_{max}k) = \cos k(x+x_0)/k$. Substituting the above equations into (3.3), the mobility is written as

$$M_{ij}^{(1)} = \frac{1}{k}\int_{x=-\infty}^{\infty}\cos k(x+x_0)\underbrace{\int_{y=-\infty}^{\infty}\left(\hat{\sigma}_{jz}\frac{\partial u_i^{(0)}}{\partial z}\right)\Big|_{z=0}\mathrm{d}y}_{m_{ij}^{(1)}}\mathrm{d}x, \tag{A14}$$

where $i,j = 1,2,\ldots,6$. For $i,j = 1,2,3$, solutions (A7) and (A8) are used to describe the sphere motion driven by a force along the x-, y- and z-directions, respectively. For $i,j = 4,5,6$, solutions (A12) and (A13) are used to describe the sphere motion driven by a torque.

Appendix B. Inversion of the resistance matrix

Falade & Brenner (1988) have derived the Stokes resistance of a sphere moving near a curved wall of small curvature. Their analysis requires that $a\kappa \ll 1$ and $h\kappa \ll 1$, meaning the sphere radius a and the distance h are small compared with the radius of curvature of the wall $1/\kappa$. We have used their results to calculate the mobility matrix. The hydrodynamic force and torque on the sphere are linked to the sphere velocity by

$$\begin{pmatrix} F/6\pi\mu a \\ T/8\pi\mu a^2 \end{pmatrix} = \boldsymbol{R} \cdot \begin{pmatrix} \boldsymbol{U} \\ \boldsymbol{\Omega} \end{pmatrix}, \tag{B1}$$

where the resistance matrix

$$\boldsymbol{R} = \begin{pmatrix} \boldsymbol{R}_t & \frac{4}{3}\boldsymbol{R}_c^{\mathrm{T}} \\ \boldsymbol{R}_c & \boldsymbol{R}_r \end{pmatrix}, \tag{B2}$$

and $\boldsymbol{R}_t = \boldsymbol{R}_t^{(0)} + a\kappa \boldsymbol{R}_t^{(1)}$, $\boldsymbol{R}_r = \boldsymbol{R}_r^{(0)} + a\kappa \boldsymbol{R}_r^{(1)}$ and $\boldsymbol{R}_c = \boldsymbol{R}_c^{(0)} + a\kappa \boldsymbol{R}_c^{(1)}$ are the force resistance, torque resistance, and the cross-coupling term. Note here the results are expanded in terms of the normalized curvature $a\kappa \ll 1$.

The mobility matrix in (3.4) can be directly calculated from $\boldsymbol{R}$,

$$\boldsymbol{M} = \begin{pmatrix} \frac{1}{6\pi\mu a}\boldsymbol{I} & \boldsymbol{0} \\ \boldsymbol{0} & \dfrac{1}{8\pi\mu a^2}\boldsymbol{I} \end{pmatrix} \cdot \begin{pmatrix} \boldsymbol{M}_t & -\dfrac{4}{3}\boldsymbol{M}_t \cdot \boldsymbol{R}_c^{\mathrm{T}} \cdot \boldsymbol{R}_r^{-1} \\ -\boldsymbol{M}_r \boldsymbol{R}_c \cdot \boldsymbol{R}_t^{-1} & \boldsymbol{M}_r \end{pmatrix}, \tag{B3}$$

where $\boldsymbol{M}_t$ and $\boldsymbol{M}_r$ are

$$\boldsymbol{M}_t = \boldsymbol{R}_t^{-1} - \tfrac{4}{3}\boldsymbol{R}_c^{-1} \cdot \boldsymbol{R}_r (\boldsymbol{R}_c^{-1})^{\mathrm{T}}, \quad \boldsymbol{M}_r = \boldsymbol{R}_r^{-1} - \tfrac{4}{3}(\boldsymbol{R}_c^{-1})^{\mathrm{T}} \cdot \boldsymbol{R}_t \boldsymbol{R}_c^{-1}. \tag{B4a,b}$$

The corresponding $O(1)$ and $O(a\kappa)$ resistance matrices are given by (Falade & Brenner 1988)

$$\left.\begin{aligned} \boldsymbol{R}_t^{(0)} &= \begin{pmatrix} A_0 & 0 & 0 \\ 0 & A_0 & 0 \\ 0 & 0 & B_0 \end{pmatrix}, \quad \boldsymbol{R}_r^{(0)} = \begin{pmatrix} C_0 & 0 & 0 \\ 0 & C_0 & 0 \\ 0 & 0 & D_0 \end{pmatrix}, \quad \boldsymbol{R}_c^{(0)} = \begin{pmatrix} 0 & E_0 & 0 \\ -E_0 & 0 & 0 \\ 0 & 0 & 0 \end{pmatrix}, \\ \boldsymbol{R}_t^{(1)} &= \begin{pmatrix} A_1 & 0 & 0 \\ 0 & B_1 & 0 \\ 0 & 0 & C_1 \end{pmatrix}, \quad \boldsymbol{R}_r^{(1)} = \begin{pmatrix} D_1 & 0 & 0 \\ 0 & E_1 & 0 \\ 0 & 0 & F_1 \end{pmatrix}, \quad \boldsymbol{R}_c^{(1)} = \begin{pmatrix} 0 & -G_1 & 0 \\ H_1 & 0 & 0 \\ 0 & 0 & 0 \end{pmatrix}. \end{aligned}\right\} \tag{B5}$$

When the sphere is far away from the surface, $a/h \ll 1$, the coefficients are

$$A_0 = 1 + \frac{9a}{16h}, \quad B_0 = 1 + \frac{9a}{8h}, \quad C_0 = 1 + \frac{9a^3}{16h^3}, \quad D_0 = 1 + \frac{a^3}{8h^3}, \quad E_0 = \frac{3a^4}{32h^4}, \tag{B6a–e}$$

$$\left.\begin{aligned} A_1 = \frac{81}{128}, \quad B_1 = \frac{27}{128}, \quad C_1 = \frac{9}{32}, \\ D_1 = E_1 = F_1 = 0, \quad G_1 = \frac{9a}{128h}, \quad H_1 = \frac{27a}{128h}. \end{aligned}\right\} \tag{B7}$$

For a sphere in near-contact with the wall, $(h-a)/a \ll 1$, the coefficients are

$$\left.\begin{gathered} A_0 = -\frac{8}{15}\ln\delta + 0.9588, \quad B_0 = \frac{1}{\delta} - \frac{1}{5}\ln\delta + 0.97128, \\ C_0 = -\frac{2}{5}\ln\delta + 0.3817, \quad D_0 = \zeta(3) - \frac{1}{2}\delta\ln\delta, \quad E_0 = -\frac{1}{10}\ln\delta - 0.1895, \end{gathered}\right\} \tag{B8}$$

$$\left.\begin{gathered} A_1 = -\frac{74}{75}\ln\delta - 0.6131, \quad B_1 = -\frac{26}{75}\ln\delta - 0.2876, \\ C_1 = \frac{1}{\delta} - 0.2001\delta^{-1/2} - 1.5613\ln\delta, \quad D_1 = -\frac{13}{50}\ln\delta - 0.6283, \\ E_1 = -\frac{7}{50}\ln\delta - 0.3951, \quad F_1 = 0.1796 - 2.2232\delta, \\ G_1 = -\frac{19}{100}\ln\delta - 0.5266, \quad H_1 = -\frac{1}{100}\ln\delta + 1.0374. \end{gathered}\right\} \tag{B9}$$

Substituting the above equations into (B3), we can derive the $O(1)$ and $O(a\kappa)$ mobility coefficients consistent with the current results requiring $A_{max}k \ll 1$ and $kh \ll 1$.

References

Assoudi, R., Chaoui, M., Feuillebois, F. & Allouche, H. 2018 Motion of a spherical particle along a rough wall in a shear flow. *Z. Angew. Math. Phys.* **69** (5), 1–30.

Bechert, D.W. & Bartenwerfer, M. 1989 The viscous flow on surfaces with longitudinal ribs. *J. Fluid Mech.* **206**, 105–129.

Belyaev, A.V. 2017 Hydrodynamic repulsion of spheroidal microparticles from micro-rough surfaces. *PLoS ONE* **12** (8), e0183093.

Berke, A.P., Turner, L., Berg, H.C. & Lauga, E. 2008 Hydrodynamic attraction of swimming microorganisms by surfaces. *Phys. Rev. Lett.* **101** (3), 038102.

Bhagat, A.A.S., Bow, H., Hou, H.W., Tan, S.J., Han, J. & Lim, C.T. 2010 Microfluidics for cell separation. *Med. Biol. Engng Comput.* **48** (10), 999–1014.

Blake, J.R. & Chwang, A.T. 1974 Fundamental singularities of viscous flow. *J. Engng Maths* **8** (1), 23–29.

Brenner, H. 1961 The slow motion of a sphere through a viscous fluid towards a plane surface. *Chem. Engng Sci.* **16** (3–4), 242–251.

Brenner, H. 1962 Effect of finite boundaries on the stokes resistance of an arbitrary particle. *J. Fluid Mech.* **12** (1), 35–48.

Cha, H., Fallahi, H., Dai, Y., Yuan, D., An, H., Nguyen, N. & Zhang, J. 2022 Multiphysics microfluidics for cell manipulation and separation: a review. *Lab on a Chip* **22** (3), 423–444.

Chastel, T. & Mongruel, A. 2016 Squeeze flow between a sphere and a textured wall. *Phys. Fluids* **28** (2), 023301.

Chwang, A.T. & Wu, T.Y. 1975 Hydromechanics of low-Reynolds-number flow. Part 2. Singularity method for stokes flows. *J. Fluid Mech.* **67** (4), 787–815.

Cooley, M.D.A. & O'Neill, M.E. 1969 On the slow motion generated in a viscous fluid by the approach of a sphere to a plane wall or stationary sphere. *Mathematika* **16** (1), 37–49.

Cox, R.G. & Brenner, H. 1967 The slow motion of a sphere through a viscous fluid towards a plane surface–II. Small gap widths, including inertial effects. *Chem. Engng Sci.* **22** (12), 1753–1777.

Dean, W.R. & O'Neill, M.E. 1963 A slow motion of viscous liquid caused by the rotation of a solid sphere. *Mathematika* **10** (1), 13–24.

Di Carlo, D., Irimia, D., Tompkins, R.G. & Toner, M. 2007 Continuous inertial focusing, ordering, and separation of particles in microchannels. *Proc. Natl Acad. Sci. USA* **104** (48), 18892–18897.

Elfring, G.J. 2017 Force moments of an active particle in a complex fluid. *J. Fluid Mech.* **829**, R3.

Falade, A. & Brenner, H. 1988 First-order wall curvature effects upon the stokes resistance of a spherical particle moving in close proximity to a solid wall. *J. Fluid Mech.* **193**, 533–568.

Faxén, H. 1922 Der widerstand gegen die bewegung einer starren kugel in einer zähen flüssigkeit, die zwischen zwei parallelen ebenen wänden eingeschlossen ist. *Ann. Phys.* **373** (10), 89–119.

GANATOS, P., PFEFFER, R. & WEINBAUM, S. 1980*a* A strong interaction theory for the creeping motion of a sphere between plane parallel boundaries. Part 2. Parallel motion. *J. Fluid Mech.* **99** (4), 755–783.

GANATOS, P., WEINBAUM, S. & PFEFFER, R. 1980*b* A strong interaction theory for the creeping motion of a sphere between plane parallel boundaries. Part 1. Perpendicular motion. *J. Fluid Mech.* **99** (4), 739–753.

GEORGIEV, R.N., TOSCANO, S.O., USPAL, W.E., BET, B., SAMIN, S., VAN ROIJ, R. & ERAL, H.B. 2020 Universal motion of mirror-symmetric microparticles in confined Stokes flow. *Proc. Natl Acad. Sci. USA* **117** (36), 21865–21872.

GOLDMAN, A.J., COX, R.G. & BRENNER, H. 1967 Slow viscous motion of a sphere parallel to a plane wall-i motion through a quiescent fluid. *Chem. Engng Sci.* **22** (4), 637–651.

HAPPEL, J. & BRENNER, H. 2012 *Low Reynolds Number Hydrodynamics: With Special Applications to Particulate Media*, vol. 1. Springer Science & Business Media.

ISHIMOTO, K., GAFFNEY, E.A. & SMITH, D.J. 2021 Squirmer hydrodynamics near a periodic surface topography. arXiv:2109.05528.

JEFFERY, G.B. 1915 On the steady rotation of a solid of revolution in a viscous fluid. *Proc. Lond. Math. Soc.* **2** (1), 327–338.

JEFFREY, D.J. 1982 Low-Reynolds-number flow between converging spheres. *Mathematika* **29** (1), 58–66.

JOKERST, J.C., EMORY, J.M. & HENRY, C.S. 2012 Advances in microfluidics for environmental analysis. *Analyst* **137** (1), 24–34.

KIM, S. & KARRILA, S.J. 2013 *Microhydrodynamics: Principles and Selected Applications*. Courier Corporation.

KUNERT, C., HARTING, J. & VINOGRADOVA, O.I. 2010 Random-roughness hydrodynamic boundary conditions. *Phys. Rev. Lett.* **105** (1), 016001.

KURZTHALER, C. & STONE, H.A. 2021 Microswimmers near corrugated, periodic surfaces. *Soft Matt.* **17** (12), 3322–3332.

KURZTHALER, C., ZHU, L., PAHLAVAN, A.A. & STONE, H.A. 2020 Particle motion nearby rough surfaces. *Phys. Rev. Fluids* **5** (8), 082101.

KYNCH, G.J. 1959 The slow motion of two or more spheres through a viscous fluid. *J. Fluid Mech.* **5** (2), 193–208.

LECOQ, N., ANTHORE, R., CICHOCKI, B., SZYMCZAK, P. & FEUILLEBOIS, F. 2004 Drag force on a sphere moving towards a corrugated wall. *J. Fluid Mech.* **513**, 247–264.

LI, G. & ARDEKANI, A.M. 2014 Hydrodynamic interaction of microswimmers near a wall. *Phys. Rev.* E **90** (1), 013010.

LI, G. & KOCH, D.L. 2020 Electrophoresis in dilute polymer solutions. *J. Fluid Mech.* **884**, A9.

LI, G., MCKINLEY, G.H. & ARDEKANI, A.M. 2015 Dynamics of particle migration in channel flow of viscoelastic fluids. *J. Fluid Mech.* **785**, 486–505.

LUCHINI, P., MANZO, F. & POZZI, A. 1991 Resistance of a grooved surface to parallel flow and cross-flow. *J. Fluid Mech.* **228**, 87–109.

MASOUD, H. & STONE, H.A. 2019 The reciprocal theorem in fluid dynamics and transport phenomena. *J. Fluid Mech.* **879**, P1.

MAUDE, A.D. 1961 End effects in a falling-sphere viscometer. *Br. J. Appl. Phys.* **12** (6), 293.

MAUDE, A.D. 1963 The movement of a sphere in front of a plane at low reynolds number. *Br. J. Appl. Phys.* **14** (12), 894.

MEHLING, M. & TAY, S. 2014 Microfluidic cell culture. *Curr. Opin. Biotechnol.* **25**, 95–102.

MOFFATT, H.K. 1964 Viscous and resistive eddies near a sharp corner. *J. Fluid Mech.* **18** (1), 1–18.

NAM-TRUNG, N. 2012 Micro-magnetofluidics: interactions between magnetism and fluid flow on the microscale. *Microfluid Nanofluid* **12**, 1–16.

O'NEILL, M.E. 1964 A slow motion of viscous liquid caused by a slowly moving solid sphere. *Mathematika* **11** (1), 67–74.

O'NEILL, M.E. & STEWARTSON, K. 1967 On the slow motion of a sphere parallel to a nearby plane wall. *J. Fluid Mech.* **27** (4), 705–724.

POZRIKIDIS, C. 1987 Creeping flow in two-dimensional channels. *J. Fluid Mech.* **180**, 495–514.

POZRIKIDIS, C. 2002 *A Practical Guide to Boundary Element Methods with the Software Library BEMLIB*. CRC Press.

RAD, S.H. & NAJAFI, A. 2010 Hydrodynamic interactions of spherical particles in a fluid confined by a rough no-slip wall. *Phys. Rev.* E **82** (3), 036305.

SAJEESH, P. & SEN, A.K. 2014 Particle separation and sorting in microfluidic devices: a review. *Microfluid Nanofluid* **17** (1), 1–52.

SMOLUCHOWSKI, M.V. 1911 On the mutual action of spheres which move in a viscous liquid. *Bull. Acad. Sci. Cracovie* A **1**, 28–39.

SPAGNOLIE, S.E. & LAUGA, E. 2012 Hydrodynamics of self-propulsion near a boundary: predictions and accuracy of far-field approximations. *J. Fluid Mech.* **700**, 105–147.

STIMSON, M. & JEFFERY, G.B. 1926 The motion of two spheres in a viscous fluid. *Proc. R. Soc.* A **111** (757), 110–116.

STOKES, G.G. 1901 On the effect of the internal friction of fluids on the motion of pendulums. *Trans. Camb. Phil. Soc.* **9**, 1–141.

STONE, H.A. & SAMUEL, A.D.T. 1996 Propulsion of microorganisms by surface distortions. *Phys. Rev. Lett.* **77** (19), 4102.

USPAL, W.E., ERAL, B.H. & DOYLE, P.S. 2013 Engineering particle trajectories in microfluidic flows using particle shape. *Nat. Commun.* **4** (1), 1–9.

YUAN, D., TAN, S.H., ZHAO, Q., YAN, S., SLUYTER, R., NGUYEN, N., ZHANG, J. & LI, W. 2017 Sheathless dean-flow-coupled elasto-inertial particle focusing and separation in viscoelastic fluid. *RSC Adv.* **7** (6), 3461–3469.

ZHANG, J., YAN, S., ALICI, G., NGUYEN, N., DI CARLO, D. & LI, W. 2014 Real-time control of inertial focusing in microfluidics using dielectrophoresis (dep). *RSC Adv.* **4** (107), 62076–62085.

ZHANG, J., YAN, S., YUAN, D., ALICI, G., NGUYEN, N., WARKIANI, M.E. & LI, W. 2016 Fundamentals and applications of inertial microfluidics: a review. *Lab on a Chip* **16** (1), 10–34.

ZHU, L., LAUGA, E. & BRANDT, L. 2013 Low-Reynolds-number swimming in a capillary tube. *J. Fluid Mech.* **726**, 285–311.